Development of one-shot aspheric measurement system with a Shack–Hartmann sensor

Yasunori Furukawa,[1,*] Yuichi Takaie,[1] Yoshiki Maeda,[1] Yumiko Ohsaki,[1] Seiji Takeuchi,[2] and Masanobu Hasegawa[1]

[1]*Canon Inc. Optics Technology Development Center, 23-10 Kiyohara-Kogyodanchi, Utsunomiya-shi, Tochigi 321-3298, Japan*
[2]*Canon U.S.A. Inc. Healthcare Optics Research Laboratory, 210 Broadway 3rd Floor, Cambridge, Massachusetts 02139, USA*
Corresponding author: ysnfurukawa@gmail.com

We present a measurement system for a rotationally symmetric aspheric surface that is designed for accurate and high-volume measurements. The system uses the Shack–Hartmann sensor and is capable of measuring aspheres with a maximum diameter of 90 mm in one shot. In our system, a reference surface, made with the same aspheric parameter as the test surface, is prepared. The test surface is recovered as the deviation from the reference surface using a figure-error reconstruction algorithm with a ray coordinate and angle variant table. In addition, we developed a method to calibrate the rotationally symmetric system error. These techniques produce stable measurements and high accuracy. For high-throughput measurements, a single measurement scheme and auto alignment are implemented; they produce a 4.5 min measurement time, including calibration and alignment. In this paper, we introduce the principle and calibration method of our system. We also demonstrate that our system achieved an accuracy better than 5.8 nm RMS and a repeatability of 0.75 nm RMS by comparing our system's aspheric measurement results with those of a probe measurement machine. © 2016 Optical Society of America

OCIS codes: (120.0120) Instrumentation, measurement, and metrology; (120.3940) Metrology.

http://dx.doi.org/10.1364/AO.55.008138

1. INTRODUCTION

Aspheric lenses are used to make optical products more compact, with reduced aberration. To fabricate accurate aspheric lenses, we need to measure the aspheric surface. Interferometers with null lenses or computer-generated holograms (CGH) [1,2] have been used to measure aspheric surfaces; however, these interferometers require a specific and expensive null lens or CGH depending on each asphere type, which adds to the cost of measurement. Therefore, a versatile system for the measurement of different aspheres is required. Recently, two methods have been developed for this purpose: a probe method and an optical method. The probe method [for example, an ultrahigh accurate 3-D profilometer (UA3P)] [3] can measure both aspheres and free forms; however, it is time consuming because the probe scans the surface point by point. The optical methods are classified into two categories. In one category, a sample lens under testing is mechanically moved, such that the test surface is measured part by part [for example, verifire asphere (VFA) [4,5] and aspheric stitching interferometers (ASIs)] [6,7]. These methods also a time-consuming and expensive solution because they require sophisticated stages to move the test sample accurately. In the second category, the test sample is not moved,

and examples include the sub-Nyquist Interferometer (SNI) [8,9], software-configurable optical test system (SCOTS) [10,11], and the method with a Shack–Hartmann sensor (SHS) [12,13]. The SHS is a wavefront sensor composed of a microlens array and a charge coupled device (CCD) [14]. The SNI and the method with the SHS have a limited accuracy due to retrace errors. The SCOTS may be a good solution to measure a large concave aspheric surface, but it is not suitable for measuring a convex aspheric surface because of the difficulty in detecting the diverged ray reflected from the convex aspheric surface with the sensor.

Considering the need for a low cost, high throughput, easy to use, and versatile system, we have developed the one-shot aspheric measurement system with an SHS, which covers a wide range of aspheric surfaces. Our system uses a reference surface for calibration and recovers the test surface as the deviation from the reference surface using a figure-error reconstruction algorithm with a ray coordinate and angle transformation table. Accuracy was achieved by developing a calibration method for a rotationally symmetric system error. In our system, the measurement time can be reduced by rapidly measuring both the reference surface and the test surface, while the reference surface is measured with the other method over time

in advance. In addition, expensive null lenses or CGHs are not required, and nothing moves during the one-shot measurement. For these reasons, our system is particularly advantageous in operating cost and measurement time.

This paper is organized as follows. In Section 2, we describe the principle and specification of the system. In Section 3, we introduce an algorithm to recover the test surface from the measurement data and the calibration method of the rotationally symmetrical system error. In Section 4, we present the experimental results of the aspheric surface measurement. Finally, we conclude this paper in Section 5.

2. PRINCIPLE AND SPECIFICATION

A. Principle

Figure 1 shows the configuration of the system. A beam from a laser diode with a wavelength of 640 nm is first focused on a pinhole with a diameter of 2 μm. The light from the pinhole is reflected by a beam splitter (BS), goes through the projection lens, and irradiates the aspheric surface as a spherical wavefront. The light reflected back by the aspheric surface goes through the projection lens, BS, and imaging lens and is finally detected with the SHS [14]. Both the projection lens and imaging lens use spherical lenses. The test lens is set at a conjugate position of the SHS. The ray angle is measured at each microlens by calculating the centroid of the spots on the CCD. The aspheric surface shape is calculated with the measured ray angle distribution and two types of tables explained further in Section 3.A. The SHS (SHScam_XHR, Optocraft GmbH) has an area of 24 mm × 36 mm, and the number of microlenses is 160 × 240. The interval of the microlens is 150 μm. As the optical magnification is approximately 4×, the sampling interval (spatial resolution) is 0.6 mm. All optics are carefully positioned and aligned using a low-coherence interferometric sensor (LISE LI 600, FOGALE nanotech Inc.) and the SHS.

Our system performs two calibrations to cancel the system errors. One is to measure the reference surface, which is made

with the parameters as the test surface and measured with other method, i.e., a probe measurement machine [15]. High accuracy is achieved by subtracting the reference surface data from the test surface data. Because both the light from the reference surface and test surface follow a nearly identical path, the optical system error (retrace error) is mostly canceled. After we measure both the reference surface and the test surface with our system, the test surface is calculated by the deviation. The cost of making the reference lens is inexpensive because it is made by the same manufacturing process as the test lens. The other calibration is employed for reducing the rotationally symmetric system error that remains after the former calibration is done (explained in detail in Section 3.B).

B. Measurement Sequence

The sequence to measure the aspheric surface is described below.

1. Set the reference lens and align it with the stage by observing the wavefront from the reference surface with the SHS. The moving amount of x, y shift and tilt are decided by the wavefront sensitivity, which is calculated in advance so that the difference between the measured wavefront and the wavefront calculated by the measurement of the reference surface with the other method is minimized.

2. Move the imaging lens and the reference lens in the z-direction to minimize the rotationally symmetric error of the optical system. This method is called magnification calibration and is explained in Section 3.B. Steps 1 and 2 occur at the same time.

3. Measure the ray angle distribution from the reference surface with the SHS.

4. Set the laser displacement sensor (LK-G82, Keyence Corporation) between the projection lens and the reference lens, and measure the z-position of the center of the reference surface.

5. Remove the reference lens and set the test lens to the measurement position. After that, move the test lens with the stage to the same z-position as the reference lens by measuring the z-position of the center of the test surface with the laser displacement sensor. Both lenses are carried to and set at the measurement position with a two-pronged mechanical arm (not shown in Fig. 1).

6. Align the test lens by observing the wavefront from the test surface in the same way as the reference lens in step 1.

7. Measure the ray angle distribution from the test surface with the SHS.

8. Calculate the test surface with ray angle distribution from the reference surface and the test surface. This method is explained further in Section 3.A.

Our system automatically aligns the reference and test lens by calculation using wavefront sensitivity. Unlike an interferometer, the user's alignment is not necessary because the wavefront measurement range of the SHS is wider. In addition, the system does not require complicated stages because nothing moves during the measurement, and a vibration-isolated system is not used because the SHS is not as sensitive to vibrations as interferometers. Regarding the measurement time, the reference surface measurement, steps 1 through 4, takes 2 min. The test surface measurement, steps 5 through 7, takes
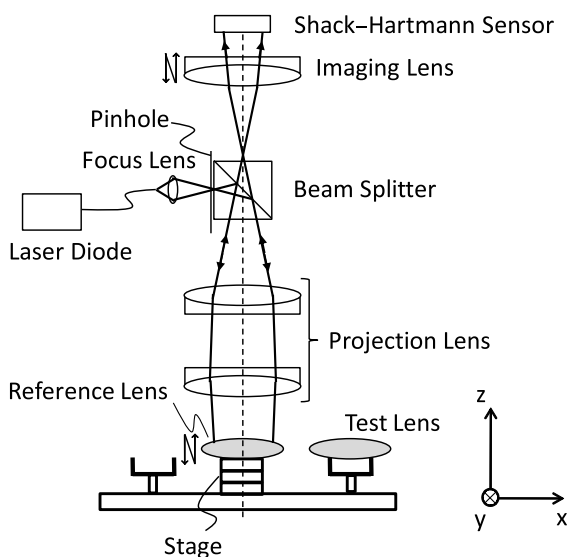

Fig. 1. Schematic layout of the optical elements in the system.

2 min. The calculation in step 8 takes 0.5 min. Thus, the total measurement time is 4.5 min for one test surface. Here the reference surface is measured every time because some lenses drift due to environmental changes such as temperature change and air turbulence, and as a result, the optical system deviates from the calibrated condition. If the environmental change is little, and the optical system keeps the calibrated condition, it is not necessary to measure the reference surface. In this case, the measurement time (steps 4 through 8) becomes 3 min.

C. Measurement Range of the Asphere

Figure 2 shows the measurement capability of the system with respect to the aspheric surface. The aspheric surfaces are shown with lines arising from the horizontal axis. The horizontal axis is the local curvature κ, calculated by Eq. (1):

$$\kappa = \left(h + \frac{r}{dh/dr} \right)^{-1}, \qquad (1)$$

where h is the asphere shape, defined by a polynomial of r, r is the radius coordinate of the asphere in the xy-plane, and $1/\kappa$ is the distance from the origin to the intersection point between the optical axis ($r = 0$) and the perpendicular line of the asphere at r which passes (r, h) (Fig. 3). When the local curvature κ is positive, the asphere is convex. When κ is negative, the asphere is concave. The vertical axis in Fig. 2 is the radius.

If the test surface is a sphere, the line is straight (solid line) because the local curvature does not change with respect to the radius. If the test surface is an asphere, the line is curved (dotted line and dashed–dotted line). The more the shape curves in the horizontal direction, the larger the asphericity (the deviation from the sphere) is. The bold, dashed line shows the measurement range of our system with one specific projection lens. Our system can measure the aspheric surface below the bold, dashed line. As we designed the optical system such that the incoming ray angle on the SHS, which is reflected by the sphere of $1/434$ mm^{-1} curvature, is zero; its curvature is the approximate center of the bold, dashed line. The height of the bold, dashed line is determined by the optical magnification, the radius of the projection lens, and the SHS area. The width of the bold, dashed line is limited by the optical magnification and incoming maximum ray angle the SHS can measure. As the optical magnification becomes larger, the measurement range becomes narrower and higher. By replacing the projection lens, the center of curvature of the measurement range can be shifted.
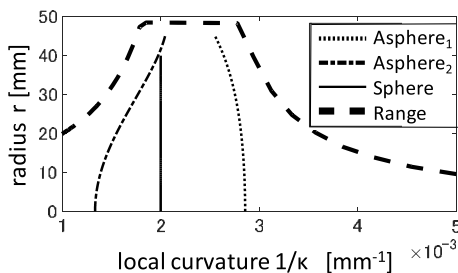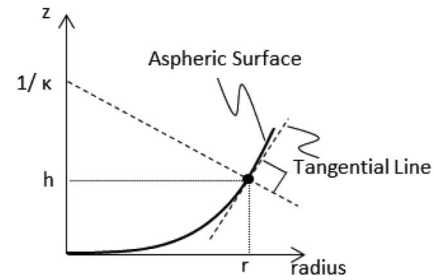

Fig. 3. Definition of the local curvature.

3. TECHNIQUE

A. Figure-Error Reconstruction Algorithm

Since a spherical wave is incident on the aspheric surface under test, the incident ray and reflected ray are not normal to the test surface. Therefore, unlike with Fizeau interferometry for flat or spherical reflective surface measurement, half of the measured optical phase delay does not provide the test surface shape. Consequently, we need to devise a calculation method to transform the direct measurement data of SHS to the test surface shape. This is done by converting the ray coordinate and angle on the SHS to those of the reflected rays from the test surface using two types of tables. The procedure for calculation is as follows:

1. The measurement by SHS provides ray angles θ_x, θ_y for each of the microlenses positioned at coordinates (x_{SHS}, y_{SHS}).

2. Calculate the meridional and sagittal angles θ_{mr}, θ_{sg} from θ_x to θ_y using Eq. (2):

$$\begin{pmatrix} \tan \theta_{mr} \\ \tan \theta_{sg} \end{pmatrix} = \begin{bmatrix} \cos \varphi & \sin \varphi \\ -\sin \varphi & \cos \varphi \end{bmatrix} \begin{pmatrix} \tan \theta_x \\ \tan \theta_y \end{pmatrix}, \qquad (2)$$

where φ is defined as Eq. (3):

$$\varphi = \tan^{-1}(y_{SHS}/x_{SHS}). \qquad (3)$$

For rotationally symmetric aspheres, it is assumed that the reflected measurement rays will be on the plane defined by the azimuthal angle φ.

3. Calculate the ray coordinate and meridional and sagittal angles on the SHS conjugate surface shown in Fig. 4 by Eqs. (4)–(6):
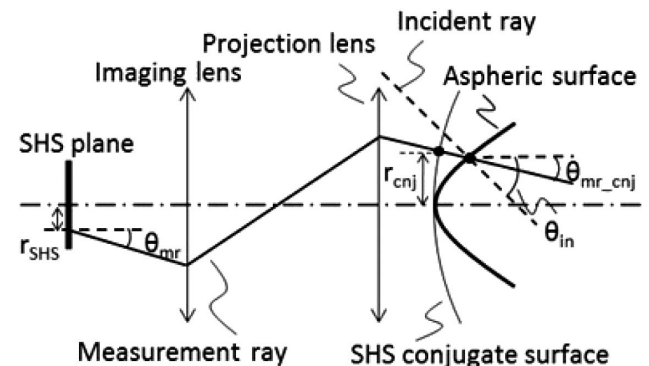

Fig. 2. Measurement range of the system about the aspheric surface.

Fig. 4. Schematic drawing of the coordinate and angle of ray in the meridional plane.

$$r_{\mathrm{cnj}} = \alpha \times r_{\mathrm{SHS}} = \alpha \times \sqrt{x_{\mathrm{SHS}}^2 + y_{\mathrm{SHS}}^2}, \tag{4}$$

$$\theta_{\mathrm{mr\_cnj}} = -(\theta_{\mathrm{mr}} - \theta_{\mathrm{mr0}})/\beta + \theta_{\mathrm{mr0\_cnj}}, \tag{5}$$

$$\theta_{\mathrm{sg\_cnj}} = -\theta_{\mathrm{sg}}/\beta. \tag{6}$$

Here, α is the coordinate table which describes the relationship between the SHS coordinate and the SHS conjugate coordinate. r_{SHS} is the distance of the measured ray on the SHS from the optical axis. r_{cnj} is the distance on the SHS conjugate surface from the optical axis. β is the angle variant table calculated from the ratio between the ray angle change on the SHS and on SHS conjugate surface. θ_{mr0} and $\theta_{\mathrm{mr0\_cnj}}$ are the ray meridional angles on the SHS surface and on the SHS conjugate surface, respectively, calculated in advance when the ray is reflected by the aspheric surface from the design. $\theta_{\mathrm{mr\_cnj}}$ and $\theta_{\mathrm{sg\_cnj}}$ are the meridional and sagittal angles on the SHS conjugate surface, respectively. The coordinate table α and the angle variant table β are calculated from the design of the aspheric surface in advance. Specifically, the reflection ray when the spherical wavefront is incident on the aspheric surface is traced in optical simulation software. For α, the ratio of ray height r_{cnj} on the SHS conjugate surface to the ray height r_{SHS} on the SHS surface is determined for each microlens of the SHS. The SHS conjugate surface is a sphere with a curvature of $1/600 \ \mathrm{mm}^{-1}$, which is imaged onto the SHS surface by the projection lens and imaging lens. Two tables α and β depend on the aspheric surface from the design. As an example, α and β are shown in Fig. 5 when the test surface is asphere$_1$ in Fig. 2. They are calculated in advance and stored as tables.

4. Calculate the crossing point of the ray whose coordinate is r_{cnj} and meridional angle is $\theta_{\mathrm{mr\_cnj}}$ on the SHS conjugate surface and aspheric surface from the design. The x, y coordinates of the cross points on the aspheric surface are assumed to be (x_s, y_s).

5. Calculate the normal angle of the aspheric surface on the (x_s, y_s) coordinates with the meridional incident ray angle (θ_{in}) to the aspheric surface, which is calculated in advance, and angles of Eqs. (5) and (6) by Eqs. (7) and (8):

$$\theta_{\mathrm{mr\_surf}} = (\theta_{\mathrm{mr\_cnj}} + \theta_{\mathrm{in}})/2, \tag{7}$$

$$\theta_{\mathrm{sg\_surf}} = \theta_{\mathrm{sg\_cnj}}/2. \tag{8}$$

6. Calculate the x and y slopes on the aspheric surface coordinate (x_s, y_s) by Eq. (9):

$$\begin{pmatrix} \tan\theta_{x\_\mathrm{surf}} \\ \tan\theta_{y\_\mathrm{surf}} \end{pmatrix} = \begin{bmatrix} \cos\varphi & -\sin\varphi \\ \sin\varphi & \cos\varphi \end{bmatrix} \begin{pmatrix} \tan\theta_{\mathrm{mr\_surf}} \\ \tan\theta_{\mathrm{sg\_surf}} \end{pmatrix}. \tag{9}$$
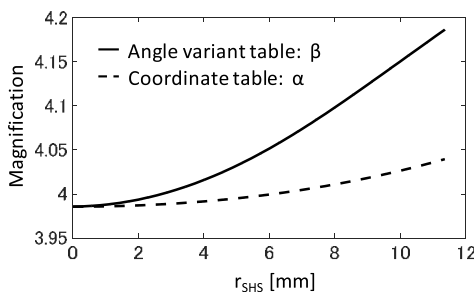

Fig. 5. Coordinate table and angle variant table.

The slope is equal to the derivative of the aspheric surface. We calculate Eqs. (2)–(9) in regard to both the reference and test measurement data and obtain the slope difference by subtracting the reference slope from the test slope.

7. Integrate the slope difference two-dimensionally with the zonal or modal method [16].

8. Add the reference surface shape, which is measured by other methods, to the integrated data to obtain the test surface shape.

B. Calibration of Rotationally Symmetrical System Error

Our optical system is composed of several lenses, which have a setting error in the z-direction, curvature error of the surface, thickness error, and so on. Moreover, the setting error changes with temperature. These (system) errors cause the measurement surface shape error of rotational symmetry. In general, system errors can be calibrated by subtracting the reference measurement data from the test measurement data. However, we found it was not enough. There are two reasons to consider. One is that the measurement shape error is sensitive to these system errors because the wavefront measured by the SHS is huge. The other reason is that since the measured reference wavefront is different from the calculated design wavefront, the tables explained in Section 3.A are also different from the actual ones. As a result, it leads to the measurement shape error. Therefore, we implemented a magnification calibration method in which these errors are minimized by moving two or three optical parts in the z-direction to conform the measured wavefront to the calculated wavefront of the reference aspheric surface. Optical parts that move are the SHS and a part of the projection lens, imaging lens, or reference lens, etc., and optical parts whose wavefront z-sensitivities are different from each other have to be chosen. For example, when the imaging lens and reference lens are assumed to be moved, each moving amount, M_{img} and M_{ref}, respectively, is determined, such that the length of the vector

$$\begin{bmatrix} W_{4m} - W_{4c} \\ W_{9m} - W_{9c} \\ W_{16m} - W_{16c} \end{bmatrix} - \begin{bmatrix} S_{4\mathrm{img}} & S_{4\mathrm{ref}} \\ S_{9\mathrm{img}} & S_{9\mathrm{ref}} \\ S_{16\mathrm{img}} & S_{16\mathrm{ref}} \end{bmatrix} \begin{pmatrix} M_{\mathrm{img}} \\ M_{\mathrm{ref}} \end{pmatrix} \tag{10}$$

is minimized, where W_{4m}, W_{9m}, and W_{16m} are the fringe Zernike 4, 9, and 16 coefficients [17] of the measured wavefront of the reference surface, respectively. For fringe Zernike polynomials of N^2th (N is 2, 3, 4 …) term, Z_N^2 is a function to express the wavefront as

$$Z_{N^2} = \sum_{i=1}^{N} (-1)^{i+1} \frac{(2N - i - 1)!}{(i - 1)!(N - i)!^2} R^{2(N-i)}, \tag{11}$$

where R is a radius on the SHS whose maximum value is normalized to units. W_{4c}, W_{9c}, and W_{16c} are fringe Zernike polynomials Z_4, Z_9, and Z_{16}, coefficients of the wavefront calculated with the asphere of the reference surface shape measured by other methods. $S_{4\mathrm{img}}$, $S_{9\mathrm{img}}$, and $S_{16\mathrm{img}}$ and $S_{4\mathrm{ref}}$, $S_{9\mathrm{ref}}$, and $S_{16\mathrm{ref}}$ are changes of the fringe Zernike polynomials Z_4, Z_9, and Z_{16}, which are coefficients when the imaging lens and the reference lens are moved in the z-direction, respectively, which is often called sensitivity. When the imaging lens and the reference lens are moved, the drive precision is not

necessary, and a resolution of 1 µm is enough. In the experiment, the length of the vector of Eq. (10) is minimized by measuring the wavefront and moving two lenses a few times. We do not know the exact system errors; however, we can make a pseudo-optical system in which the system errors are canceled by moving the imaging lens and the reference lens. Therefore, even if there are some errors of the optical system, the test aspheric surface can be obtained accurately by measuring the reference and test surfaces after moving.

We set up a simulation to confirm the effect of magnification calibration. First, we assumed that the reference surface was the aspheric design value, which is shown in Fig. 2 as the dashed–dotted line (Asphere$_2$), and the test surface had a surface shape error defined by the fringe Zernike 25th, with a coefficient of 450 nm. In addition, we assumed approximately 100 nm PV surface errors of multiple lens surfaces and 70–200 µm lens spacing errors of the optical system to imitate the real errors. Second, we calculated the ray angle distribution on the SHS plane, which was reflected by the reference surface, and passed through the optical system, and obtained the wavefront difference $(W_{4m} - W_{4c}, W_{9m} - W_{9c}, W_{16m} - W_{16c})$. Third, after we moved the imaging lens and the reference surface by the amount calculated by Eq. (10), we calculated the ray angle distribution on the SHS plane, which was reflected by the reference surface and the test surface and passed through the above optical system. Finally, we calculated the test surface shape using the method described in Section 3.A.

Figure 6 is the calculated measurement error, which indicates the difference from the input shape (450 nm × fringe Zernike Z_{25}) of the test surface. Figure 6(a) indicates that when there are multiple errors of the optical system, they cause the shape measurement error (4.0 nm RMS). Figure 6(b) shows the shape measurement error applied with the magnification calibration, which is 0.82 nm RMS. From these two results, the shape measurement error is found to be decreased by the magnification calibration. This method eases the error budget of the system, including the manufacturing error, setting error of the optical system, mechanical drift, position error by temperature change, and so on.

4. EXPERIMENT

To verify the performance of our system, we measured the aspheric surface and compared the results with those obtained using a probe measurement machine [15]. The asphere we used for verification is shown by the dotted line (Asphere$_1$) in Fig. 2. The asphere's diameter is 90 mm, the deviation from the sphere is 39 µm, and the center of curvature is $1/350$ mm^{-1}. We used a reference surface measured with the probe measurement machine.

Figure 7(a) shows the measurement with our system, which is the deviation from the design value. The sampling intervals Δx and Δy are 0.6 mm. Figure 7(b) shows the result obtained by the probe measurement machine. The lateral coordinate of Fig. 7(b) is the same as that of Fig. 7(a). Figure 7(b) is obtained by applying the triangle-based cubic interpolation [18] to the probe measurement data, whose sampling intervals Δx and Δy are 0.2 and 0.1 mm, respectively. The shape errors due to an alignment error of the test surface, which are the x-tilt (Z_2), y-tilt (Z_3), defocus (Z_4), x-shift, and y-shift, are removed from these measurement data by fitting with them. Here, the alignment error due to the x- or y-shift is calculated by $h(x + 1 \text{ µm}, y) - h(x, y)$ or $h(x, y + 1 \text{ µm}) - h(x, y)$, where h is the designed aspheric shape. The height cross sections in the x-directions of both results [Figs. 7(a) and 7(b)] are shown in Fig. 7(c). These measurement results indicate that the shape error is approximately 800 nm PV and qualitatively correspond to each other. Figure 7(d) shows the difference between the two measurement results [Figs. 7(a) and 7(b)], and the difference is 5.8 nm RMS. The estimated measurement error of our optical system alone is 3.9 nm RMS. Considering that the experimental measurement error includes the error of the probe measurement machine, it seems that this experimental result is valid. The accuracy of the probe measurement is known to be better than 5.8 nm RMS. In addition, since 5.8 nm RMS includes both the reference and the test surface measurement errors of the probe measurement machine, we can conclude that
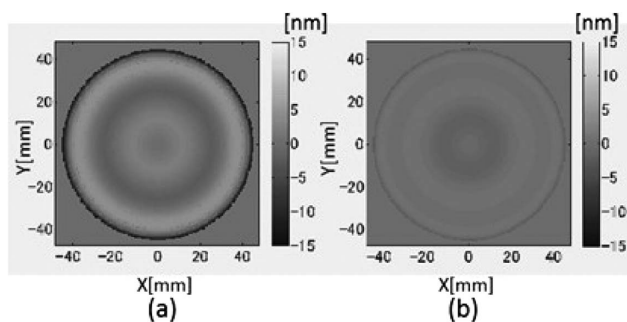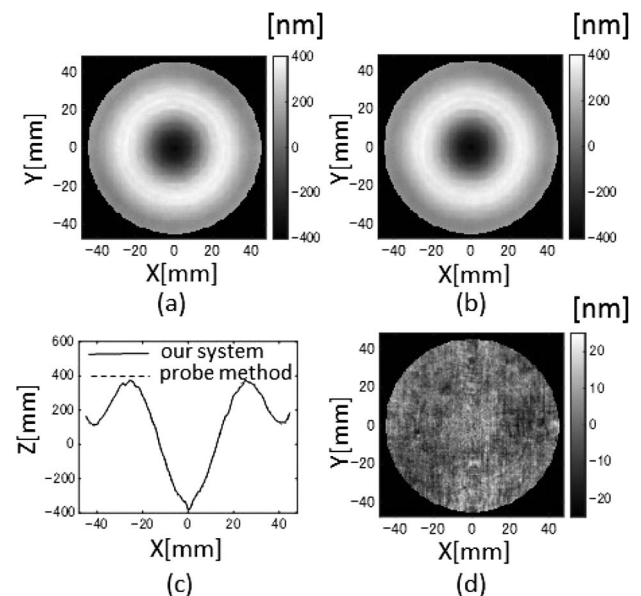

Fig. 6. Shape measurement error due to system errors (simulation results). (a) Without magnification calibration. (b) With magnification calibration.

Fig. 7. Measurement results of the aspheric surface with our system (a) and probe measurement machine (b). (c) Height cross-sectional data in the x-direction in (a) and (b). (d) Differences between the two measurement results.
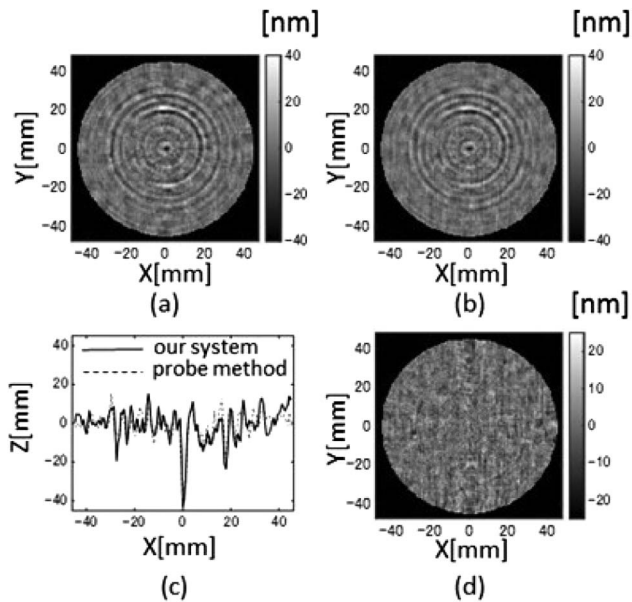
Fig. 8. Measurement results of the aspheric surface of spatially high frequency component with our system (a) and probe measurement machine (b). (c) Height cross-sectional data in the x-direction in (a) and (b). (d) Differences between the two measurement results.

Fig. 9. Repeatability of the aspheric measurement.

the accuracy of our system (including the reference surface error) is better than 5.8 nm RMS.

To verify the accuracy of the high spatial-frequency component, we subtracted the Zernike fitting data from measurement data [Figs. 7(a) and 7(b)]. In Fig. 8(a), fringe Zernike 169 components are subtracted from the measurement data [Fig. 7(a)] obtained by our system. This is the high spatial-frequency component. Figure 8(b) shows the one obtained by the probe measurement machine. In both figures, similar concentric circular grinding marks can be seen. Height cross sections in x-directions of both results [Figs. 8(a) and 8(b)] are shown in Fig. 8(c). From Fig. 8(c), we can see a central concavity in both results, and they correspond to each other. Figure 8(d) is the difference between the two results. The difference between the two measurement results is 4.7 nm RMS. As there are no concentric circular grinding marks or central concavity in Fig. 8(d), we can see that the form achieved by our system agrees well with the one produced by the probe measurement machine with a high spatial-frequency component.

To evaluate the repeatability, we implemented the sequence described in Section 2.B and measured the test surface fifty times. Figure 9 shows the RMS difference from the average of fifty measurements, which is calculated by Eq. (12):

$$\sigma_j = \sqrt{\sum_{x,y} \left\{ S(x,y;j) - \sum_{i=1}^{N} S(x,y;i)/N \right\}^2 / n}, \quad \textbf{(12)}$$

where j is an integer equal to or less than fifty, $S(x,y;j)$ is the jth test surface measurement data, N is fifty, and n is the number of pixels in the data. When repeatability is defined as the average of σ, the repeatability of our system is 0.75 nm RMS. The air
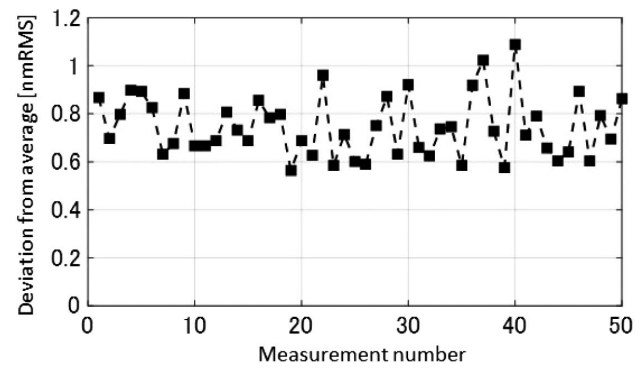
fluctuation and CCD noise are estimated to be the main errors of repeatability.

5. CONCLUSIONS

We developed an aspheric surface measurement system with an SHS that has the versatility to measure various aspheres. Our system achieved high accuracy through the development of an algorithm to recover the test surface shape with a ray coordinate and angle variant table and a calibration method to cancel the rotationally symmetrical system error. From the experiment, we confirmed that our system has the following: high throughput, 4.5 min; high accuracy, <5.8 nm RMS; and high repeatability, 0.75 nm RMS. As the procedures of the calibration and alignment of the test lens are executed automatically, the user can measure the aspheric surface with just the push of a button. Therefore, it is our expectation that our system will be used in the inspection and manufacturing of high-volume aspheric lenses or mirrors. One drawback is that our system requires the aspheric reference surface data measured with other methods for calibration. It means our system depends on and is limited by the accuracy of the reference measurement method. Hence, we intend to develop a calibration method without the aspheric reference surface data, so that our system can also be used for small-lot optical products.

REFERENCES

1. J. C. Wyant and V. P. Bennett, "Using computer generated holograms to test aspheric wavefronts," Appl. Opt. **11**, 2833–2839 (1972).
2. A. G. Poleshchuk, R. K. Nasyrov, and J. M. Asfour, "Combined computer-generated hologram for testing steep aspheric surfaces," Opt. Express **17**, 5420–5425 (2009).
3. H. Tsutsumi, K. Yoshizumi, and H. Takeuchi, "Ultrahighly accurate 3D profilometer," Proc. SPIE **5638**, 387–394 (2005).
4. M. F. Kuechel, "Absolute measurement of rotationally symmetric aspheric surfaces," in *Optical Fabrication and Testing* (Optical Society of America, 2006), paper OFTuB5.
5. M. F. Kuechel, "Interferometric measurement of rotationally symmetric aspheric surfaces," Proc. SPIE **7389**, 738916 (2009).
6. P. Murphy, G. DeVries, J. Fleig, G. Forbes, A. Kulawiec, and D. Miladinovic, "Measurement of high-departure aspheric surfaces using

subaperture stitching with variable null optics," Proc. SPIE **7426**, 74260P (2009).

7. C. Supranowitz, C. McFee, and P. Murphy, "Asphere metrology using variable optical null technology," Proc. SPIE **8416**, 841604P (2012).

8. J. E. Greivenkamp, "Sub-Nyquist interferometry," Appl. Opt. **26**, 5245–5258 (1987).

9. J. E. Greivenkamp, A. E. Lowman, and R. J. Palum, "Sub-Nyquist interferometry: implementation and measurement capability," Opt. Eng. **35**, 2962–2969 (1996).

10. P. Su, R. E. Parks, L. Wang, R. P. Angel, and J. H. Burge, "Software configurable optical test system: a computerized reverse Hartmann test," Appl. Opt. **49**, 4404–4412 (2010).

11. P. Su, R. E. Parks, L. Wang, R. P. Angel, and J. H. Burge, "SCOTS: a quantitative slope measuring method for optical shop use," in *Optical Fabrication and Testing* (Optical Society of America, 2010), paper OTuB3.

12. J. Pfund, N. Lindlein, and J. Schwider, "Non-null testing of aspherical surfaces by using a Shack–Hartmann sensor," in *Optical Fabrication and Testing* (Optical Society of America, 2000), paper OTuC5.

13. J. Pfund, N. Lindlein, and J. Schwider, "Non-null testing of rotationally symmetric aspheres: a systematic error assessment," Appl. Opt. **40**, 439–446 (2001).

14. I. Gozeil, "Hartmann and other screen tests," in *Optical Shop Testing*, D. Malacara, ed. (Wiley, 1978), Chap. 10, pp. 323–349.

15. M. Negishi, "Development of a high precision free-form measurement machine," J. Jpn. Soc. Precis. Eng. **67**, 1632–1636 (2001).

16. W. H. Southwell, "Wave-front estimation from wave-front slope measurements," J. Opt. Soc. Am. **70**, 998–1006 (1980).

17. Cited 10 April, 2016, http://www.cybernet.co.jp/optical/course/word/s17.html.

18. T. Y. Yang, *Finite Element Structural Analysis* (Prentice-Hall, 1986), pp. 446–449.